RESEARCH ARTICLE

Author Contributions:
Conceptualization: Erica Mariani, Sev Kender
Investigation: Erica Mariani, Sev Kender, Melanie J. Leng, Simon J. Kemp, Thomas Wagner, Alexander J. Dickson
Resources: Karen Dybkjær, Gunver K. Pedersen
Supervision: Sev Kender, James B. Riding
Visualization: Erica Mariani, Sev Kender
Writing – original draft: Erica Mariani, Sev Kender, Stephen P. Hesselbo, Kara Bogus, Kate Littler, James B. Riding, Melanie J. Leng, Simon J. Kemp,

Large Igneous Province Control on Ocean Anoxia and Eutrophication in the North Sea at the Paleocene–Eocene Thermal Maximum

Erica Mariani[1] , Sev Kender[1,2] , Stephen P. Hesselbo[1,3] , Kara Bogus[1], Kate Littler[1,3], James B. Riding[2], Melanie J. Leng[2] , Simon J. Kemp[2] , Karen Dybkjær[4] , Gunver K. Pedersen[4], Thomas Wagner[5] , and Alexander J. Dickson[6]

[1]Camborne School of Mines, Department of Earth and Environmental Sciences, University of Exeter, Cornwall, UK, [2]British Geological Survey, Nottingham, UK, [3]Environment and Sustainability Institute, University of Exeter, Cornwall, UK, [4]Geological Survey of Denmark and Greenland (GEUS), Copenhagen, Denmark, [5]Lyell Centre, Heriot-Watt University, Edinburgh, UK, [6]Department of Earth Sciences, Royal Holloway, University of London, Surrey, UK

Abstract The Paleocene–Eocene Thermal Maximum (PETM) was a global hyperthermal event ∼56 Ma characterized by massive input of carbon into the ocean–atmosphere system and global warming. A leading hypothesis for its trigger is the emplacement of the North Atlantic Igneous Province (NAIP), with extensive extrusion/intrusion of igneous material into nearby sedimentary basins, forcing local uplift and warming-inducing carbon emissions. It remains unclear if oceanographic changes in the North Sea–Norwegian Sea–Arctic basins, such as anoxia and productivity, were causally linked to local NAIP uplift/activity, and at what time scales these perturbations occurred. To test mechanisms and time scales, we present geochemical proxies (XRF analysis, clay mineralogy, molybdenum isotopes, and pyrite framboid size distribution) in undisrupted marine sediment core E−8X located in the central North Sea. We find evidence for a rapid onset of anoxia/euxinia at the negative carbon isotope excursion from redox proxies, followed by a gradual drawdown of molybdenum/total organic carbon (Mo/TOC) during the PETM main phase indicative of tectonically-restricted basin likely from NAIP uplift. A short-lived increase in Mo, pyrite and TOC occurred during a precursor event associated with a sedimentary mercury pulse indicative of volcanic activity. We suggest thermal uplift and flood basalt volcanism tectonically restricted the North Sea and tipped it into an euxinic state via volcanic emission–oceanographic feedbacks inducing eutrophication. This fine temporal separation of tectonic versus climatic geochemical proxies, combined with pulsed NAIP volcanism, demonstrates that Large Igneous Province emplacements can, at least locally, result in ocean biogeochemical feedbacks operating on relatively short timescales.

1. Introduction

The Paleocene-Eocene Thermal Maximum (PETM) was a global warming event ∼56 Ma that led to anomalous sea surface temperature increases of ∼5–9°C (Dunkley Jones et al., 2013). The PETM is associated with injections of ^{13}C-depleted carbon into the exogenic carbon pool, reflected in a 2–7‰ negative carbon isotope excursion (CIE) in marine and terrestrial sediment successions. The relative age model of the event encompassing the CIE onset and recovery phases is based on two proposed cyclostratigraphic solutions from Svalbard core BH9/05, whose durations are estimated to be ∼140 ka (option A) and ∼200 ka (option B) (Charles et al., 2011). The overall event and its rapid onset of ∼3–4 kyr (Kirtland Turner et al., 2017; Kender et al., 2021) can be used to test climate models and to predict, within limitations, how climate might respond to anthropogenic activity. However, the causal mechanisms triggering the PETM are still unclear, hampering our ability to model the consequences of the event at the local scale.

The PETM affected marine environments by reducing water column oxygenation in many locations from high to low northern and southern latitudes, the paleo-Tethys, Europe, Asia, and America (Carmichael et al., 2017; Papadomanolaki et al., 2022). The PETM onset is associated with the largest Mesozoic–Cenozoic benthic foraminiferal extinction (Thomas, 1998). Multiple causal factors have been proposed, such as temperature increase leading to high metabolic rates in starved waters from increased organic matter remineralization (Ma et al., 2014), ocean acidification (Thomas, 2007), and oxygen depletion (Thomas, 1998). In NW Europe, particularly around the North Sea, Denmark, Norway, and Arctic Ocean, laminated sediments and organic

Karen Dybkjær, Gunver K. Pedersen, Thomas Wagner, Alexander J. Dickson
Writing – review & editing:
Erica Mariani, Sev Kender, Stephen P. Hesselbo, Kara Bogus, Kate Littler, James B. Riding, Melanie J. Leng, Karen Dybkjær, Gunver K. Pedersen, Thomas Wagner, Alexander J. Dickson

geochemical proxies have been recorded suggesting widespread anoxia during the PETM (Berndt et al., 2023; Harding et al., 2011; Kender et al., 2012; Schoon et al., 2015; Sluijs et al., 2006). Although increased hydrological cycling and primary production has been suggested as the main cause of oxygen depletion (Dickson, Rees-Owen, et al., 2014; Ma et al., 2014), areas proximal to the North Atlantic Igneous Province (NAIP), such as the North Sea, have been subjected to strong local environmental changes related to the emplacement of the NAIP (Kender et al., 2012). Among these changes, basin restriction of the North Sea via tectonic uplift is a favored mechanism that may have contributed to oxygen depletion in the North Sea and surrounding areas (Hartley et al., 2011).

Regional tectonic uplift was primarily controlled by the upward movement of the Icelandic mantle plume between Greenland and Scotland during the opening of the Northeast Atlantic Ocean (Hartley et al., 2011; Jones, Hoggett, et al., 2019). The correlation between tectonic uplift and NAIP activity is well documented, with thousands of intruded sills recognized in 2D and 3D seismic stratigraphy in the Norwegian Sea and northwestern North Sea (Berndt et al., 2023; Conway-Jones & White, 2022; Hartley et al., 2011; Jones, Percival, et al., 2019; Svensen et al., 2004). Increased volcanic activity around the PETM onset is also documented by sedimentary mercury (Hg) and Hg isotopes in the North Sea, Spain, Svalbard, Denmark, and the Arctic Ocean (Jin et al., 2023; Jones, Percival, et al., 2019; Kender et al., 2021; Tremblin et al., 2022). The North Sea and the northern Atlantic Ocean were connected by a shallow seaway, however this connection was possibly cut off by the NAIP uplift (Hartley et al., 2011; Zacke et al., 2009). NAIP emplacement not only modified the North Sea–North Atlantic connection, but also reorganized and narrowed the Norwegian–Greenland seaway, which became a shallow water strait around the PETM (Berndt et al., 2023; Hovikoski et al., 2021; Planke et al., 2023). Since the Norwegian–Greenland seaway was further connected to the Arctic Ocean (Prøis, 2015), the shallowing of the seaway would result in the partial isolation of the Arctic Ocean (Jones et al., 2023).

Previous records of bottom water oxygen depletion in the North Sea region are not sufficiently resolved to identify whether basin restriction facilitated, or drove, the observed anoxia/euxinia around the PETM onset (e.g., Schoon et al., 2015; Stokke et al., 2021). The exact phasing between the emplacement of the NAIP, North Sea basin restriction, primary productivity and runoff changes and bottom water anoxia/euxinia has not yet been robustly determined, mainly due to the lack of high-resolution records from high quality core material. Previous records are inconclusive due to incomplete core recovery and drilling disturbance at the CIE onset and the main PETM phase (Arctic Ocean core 302-M0004 A, Sluijs et al., 2006), or have been affected by transported organic carbon from mixed sources and/or reworked terrestrial material around the CIE onset, which may alter the shape of the CIE (North Sea core 22/10a-4, Kender et al., 2012; Longyearbyen, Svalbard, Harding et al., 2011; Svalbard core BH9/05, Cui et al., 2011). The timing of volcanic activity, basin restriction and oceanographic change is not only critical for understanding the causal mechanisms of North Sea anoxia/euxinia, but also has large implications for the tipping point of the PETM. Several lines of evidence argue that NAIP activity contributed to the trigger of the PETM carbon release, including direct proxy-based evidence for volcanism immediately preceding and during the CIE onset from high resolution sedimentary Hg (Jones, Percival, et al., 2019, 2023; Kender et al., 2021; Tremblin et al., 2022) and Hg isotope records (Jin et al., 2023). Although the correlation between tectonic uplift and volcanic activity is well documented (Champion et al., 2008; Conway-Jones & White, 2022; Hartley et al., 2011; Storey et al., 2007; Wilkinson et al., 2017), possible bottom water changes resulting from tectonically driven basin restriction need further investigation.

In this study, we analyze the evolution of hydrography and bottom water oxygen conditions with a particular focus to the PETM CIE onset, from an exceptionally well-preserved marine sediment core previously described from the Danish sector of the North Sea (wellsite E−8X; Figure 1; Kender et al., 2021). E−8X consists of undisturbed marine sediments encompassing the PETM onset, main phase and recovery intervals, and has a CIE onset that is well defined and thought to represent approximately continuous sedimentation (Kender et al., 2021). We generated geochemical data, including elemental ratios, clay mineralogy, Mo isotopes, and pyrite framboid size distribution, to determine the succession of oxygen conditions, primary productivity and terrigenous input at the transition to the PETM CIE. We use these records to investigate the lead/lag relationships between volcanic activity, carbon release, euxinia, productivity and inferred basin restriction. We find that precursor PETM basin restriction likely created the conditions for pulsed volcanism to drive initial reductions in bottom water oxygenation, followed by climate-driven productivity increases shortly after the PETM onset.
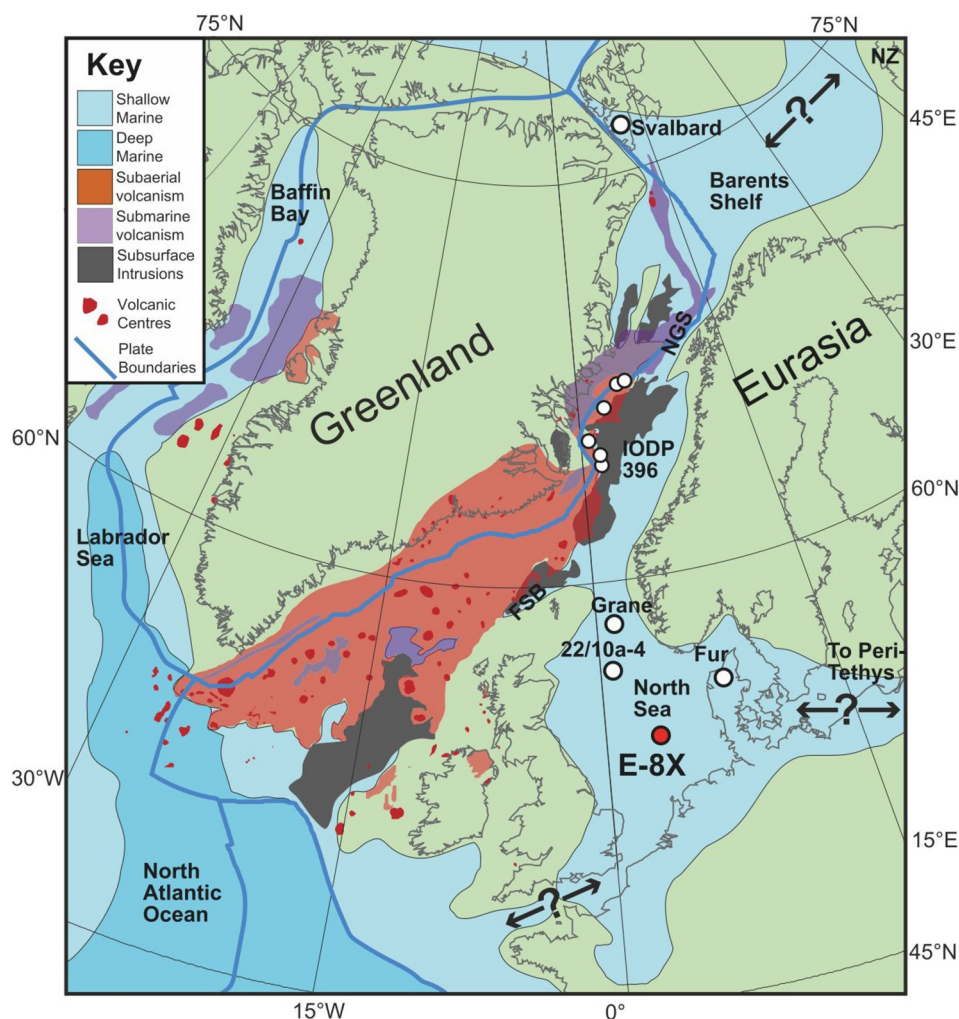
Figure 1. Late Paleocene paleogeographic reconstruction (adapted from Jones et al., 2023). the light red, violet and gray areas represent subaerial, submarine and subsurface volcanism and sill intrusions, respectively. Dark red points represent volcanic centers. Shallow and deep marine areas are shown as light and dark blue, respectively. FSB: Faroe-Shetland Basin; NGS: Norwegian-Greenland Seaway; NZ: Novaya Zemlya.

2. Material and Methods

2.1. Depositional Setting and Stratigraphy of E−8X

Wellsite E−8X (55°38'13.42''N, 04°59'11.96''E) is located in the central portion of the Danish North Sea (Figure 1) and the core is described in Kender et al. (2021). The paleobathymetry of the deep central parts of the northern North Sea (58–62°N), was reconstructed to have been around 600–800 m deep (Kjennerud & Gillmore, 2003). Since Wellsite E−8X is located only 3°S of the northern North Sea in the deep central portion of the basin, we assume that paleodepths might have not been too dissimilar, with the central part of the North Sea being >500m. The Paleocene-Eocene boundary in core E−8X was previously identified by a positive excursion on the gamma-ray log at the base of the Sele Formation, along with the acme of *Apectodinium augustum*, a dinoflagellate cyst biomarker for the PETM, located in the lowermost laminated part of the Sele Formation (Schiøler et al., 2007; Supplementary Material). The studied core interval consists of 7 m of marine sediments (2021.06–2027.36 m composite core depth) spanning the uppermost Paleocene and lowermost Eocene. The CIE (2,025.41–2,025.32 m) was identified by a 5‰ negative stable organic carbon isotope ($\delta^{13}C_{org}$) excursion in the bulk material (Kender et al., 2021), whose amplitude ‰ is consistent with the CIE expression at nearby wellsite 22/10a-4 (Kender et al., 2012).

The CIE displays a two-step trend: the first step is characterized by a persistent 1.6‰ decline in $\delta^{13}C_{org}$ values between 2,025.4 and 2,025.37 m; the second step is more rapid with an amplitude of around 3.4‰ between 2025.36 and 2025.32 m and reaches minimum $\delta^{13}C_{org}$ values of -30.7‰ (Kender et al., 2021). The "main phase" of the PETM (2,025.32–2,023.15 m) is an interval assigned to the Sele Formation (Kender et al., 2021; Fig. S1 in Supporting Information S1) with sustained negative $\delta^{13}C_{org}$ values of -31‰ to -29‰ at E−8X. The main phase is dominated by finely laminated dark mudstone, although a silty interval is observed from ∼2,024.5 to 2,023.2 m. The recovery Phase 1 (2,023.15–2,022.10 m), and Phase 2 (2,022.10–2,021.06 m) are recognized by inflection points in the $\delta^{13}C_{org}$ signal with recovery Phase 2 exhibiting higher $\delta^{13}C_{org}$ values than recovery Phase 1, albeit values across both recovery phases do not go back to pre PETM levels.

2.2. Carbon Isotopes and Total Organic Carbon

To further constrain the two-step CIE onset recognised in Kender et al. (2021), 39 new sediment samples were micro-drilled at a sample spacing of ∼5 mm (Figs. S2, S3, S4 in Supporting Information S1), covering the interval between 2,025.52 and 2,025.32 m. The $\delta^{13}C_{org}$ and total organic carbon (TOC) analyses were carried out at the NERC Isotope Geosciences Laboratory at the British Geological Survey. Inorganic carbon was removed by treating the powdered sediments with 5% HCl overnight. TOC was then determined on bulk samples by combustion in a Costech ECS4010 Elemental Analyzer calibrated against an acetanilide standard. $^{13}C/^{12}C$ analyses were performed on bulk rock samples by combustion in a Costech Elemental Analyzer on-line to a VG TripleTrap and Optima dual-inlet mass spectrometer, with $\delta^{13}C_{org}$ values relative to VPDB using three within-run laboratory standards calibrated against NBS-18, NBS-19, and NBS-22. The internal standards yield standard deviations of 0.07, 0.05, and 0.1. The additional values were incorporated into the isotope stratigraphy and TOC records of Kender et al. (2021) that were measured in the same laboratory.

2.3. X-Ray Fluorescence Spectrometry

Portable X-ray fluorescence (pXRF) measurements were performed using an Olympus DELTA Professional X-ray portable spectrometer at the Camborne School of Mines, University of Exeter, on 621 bulk rock samples to investigate major and trace elements. The pXRF analytical accuracy was checked by running Standard Reference Material 2710a every 10 samples, with values of expected and measured major element within 1% (Fig. S5 in Supporting Information S1). Samples were taken at ∼1 cm resolution and powdered with an agate pestle and mortar. Homogenised samples with thickness >5 mm were measured in glass vials with non-PVC cling film and placed in a shielded chamber that faced the analyzer measuring window. The analysis was carried out in "geochem mode" (abundance%) with a run time of 60 s to allow for reliable trace metal measurements (Dahl et al., 2013).

To constrain the pXRF data quantitatively, analyses of titanium (Ti), aluminum (Al), iron (Fe) and silicon (Si) were performed on a subset of the same samples ($n = 53$) with a conventional based XRF (bXRF; Figs. S6, S7 in Supporting Information S1). The instrument was a PANalytical Axios mAX sequential, fully automatic wavelength-dispersive X-ray fluorescence spectrometer fitted with a 60 kV generator and 4 kW rhodium (Super Sharp) end–window X-ray tube. The software used to control the instrument and report data was PANalytical SuperQ 5.2 A. The samples were prepared by taking 0.9 g of sample and mixing it with 9 g of 66:34 lithium tetraborate/lithium metaborate flux and fusing for 12 min at 1,200°C. The fused glass bead was analyzed using the Malvern Panalytical WROXI application. Background factors were calculated by either angular difference (2Ө) or from regression values from "high purity" single oxide standards. Line-overlap factors were calculated from "high purity" oxide standards of the interfering analyte on regression. The PANalytical calibration algorithm was used to fit calibration curves, deriving calibration constants for slope and concentration intercept. Inter-element effects were corrected by fundamental parameter (FP) coefficients, calculated by the PANalytical fundamental parameter method. All backgrounds and peaks were corrected for instrument drift using two external ratio monitors. Drift correction intensities from the monitors were used to monitor instrumental stability and detect machine faults. The calibrations were validated by analysis of a number of Reference Materials (Table S1 in Supporting Information S1).

Total sulfur (S) concentration analysis was performed on 25 samples using a LECO CS230 instrument at Newcastle University in duplicate after 10 samples with a RSD of 1.5%. Certified calibration carbon/S standards (0.815/0.0032%, respectively) supplied by Leco UK Ltd, along with analytical blanks were measured every 20

and 25 analytical samples, respectively. Conventional XRF data, and dilution from the ^{100}Mo/^{95}Mo, were primarily used to calibrate the pXRF data, and results were compared through regression analysis (Fig. S6 in Supporting Information S1). As pXRF data consistently underestimated Al, Si and Mo contents, we corrected these using linear regression equations (Fig. S7 in Supporting Information S1). We emphasize that our paleo-environmental reconstructions are based on relative trends rather than absolute values.

2.4. Molybdenum Isotopes and Concentrations

Molybdenum isotope analysis was performed on 18 samples, four of which were taken at 2,026.85, 2,026.5, 2,025.9, and 2,025.47 m corresponding to the pre PETM interval; the sampling resolution was increased across the CIE by analyzing five samples between 2,025.41 and 2,025.33 m, to capture any change around the CO_2 injection; five samples were selected across the PETM main phase between 2,025.29 and 2,023.5 m; two samples were taken at 2,023 and 2,022.5 m corresponding to the recovery Phase 1 interval, and two samples were chosen in the recovery Phase 2 at 2,022 and 2,021.5 m (Figs. S6, 7 in Supporting Information S1). Homogenised sample powders were mixed with a precise mass of a ^{100}Mo-^{97}Mo double spike solution and digested in a mixture of 3:1 HNO_3/HCl. Molybdenum was separated from matrix elements using the anion column method of Pearce et al. (2010) as modified by Dickson et al. (2016). Purified sample solutions were measured on a Neptune Plus MC-ICP-MS at Royal Holloway, University of London, using 10 ppb solutions introduced to the mass spectrometer via an Aridus III desolvator. Measurements consisted of $80 \times 8.4s$ integrations. Voltages were background corrected with a short measurement of 3% HNO_3 prior to each measurement. Sample-spike mixtures were solved offline using an Excel-based routine. Isotope compositions are expressed relative to NIST 3134 as:

$$\delta^{98/95}\text{Mo} = \left(\left(\frac{^{98}\text{Mo}/\ ^{95}\text{Mo}_{\text{sample}}}{^{98}\text{Mo}/\ ^{95}\text{Mo}_{\text{NIST3134}}}\right) - 1 * 1000\right) + 0.25‰$$

Uncertainties are propagated from the 2 S.E. counting statistics and the bracketing NIST 3134 solutions and are generally similar to the long-term external reproducibility of $\pm0.06‰$ determined from multiple digestions and measurements of the SDO-1 USGS shale. A sample of SDO-1 prepared in the same batch as the North Sea samples had a composition of $1.09 \pm 0.03‰$, which is identical to values from previous studies (Goldberg et al., 2013, p. $1.05 \pm 0.2‰$; Dickson et al., 2019, p. $1.04 \pm 0.08‰$). A procedural blank measured by isotope dilution was 120 pg, which is insignificant compared to the mass of Mo processed for each sample ($\sim$400–500 ng). Molybdenum concentrations were calculated by isotope dilution from the ^{100}Mo/^{95}Mo ratio.

2.5. Scanning Electron Microscopy

Thirteen samples were chosen to study the size distribution of pyrite framboids as a proxy for bottom water redox conditions, using a TESCAN VEGA3 scanning electron microscope (SEM) at Camborne School of Mines, University of Exeter. The samples were chosen so that the sample spacing throughout the main phase, recovery Phase 1 and 2 was constantly set to $\sim$30 cm to avoid sampling biases. However, this wasn't always achievable due to scarceness of rock samples available, and in some instances sample spacing spanned from $\sim$10 to $\sim$50 cm. With regards to the pre PETM interval, only two samples were chosen due to the generally low TOC and non-laminated sediments, suggesting that the pre PETM interval sedimented in mostly oxic conditions and possibly be devoid of pyrite. One pre PETM sample was chosen at $\sim$10 cm before the CIE to investigate if the onset of anoxia might have occurred before the CO_2 injection. Sediment samples were cut into sections and mounted in resin blocks, polished with diamond paste, and carbon-coated. The diameter of 100 pyrite framboid specimens per sample, a representative number selected in accordance with previous global-scale pyrite framboid studies across Permian-Triassic boundary sections (Bond & Wignall, 2010), were measured in backscattered electron mode (BSE).

2.6. Clay Mineralogy

The clay mineralogy of a total of 77 samples were investigated using X-ray diffraction (XRD) analysis at the British Geological Survey laboratories, Keyworth. About 4 g of sample was crushed and passed through a 2 mm sieve. The <2 mm fraction was then dispersed in deionized water using an ultrasonic bath and reciprocal shaker; the resulting suspension was sieved on a 63 μm sieve and placed in a 250 ml cylinder with few drops of 0.1 M Na$_6$[(PO$_3$)$_6$] to prevent flocculation and to disperse the clay particles. The suspension was left to settle for periods
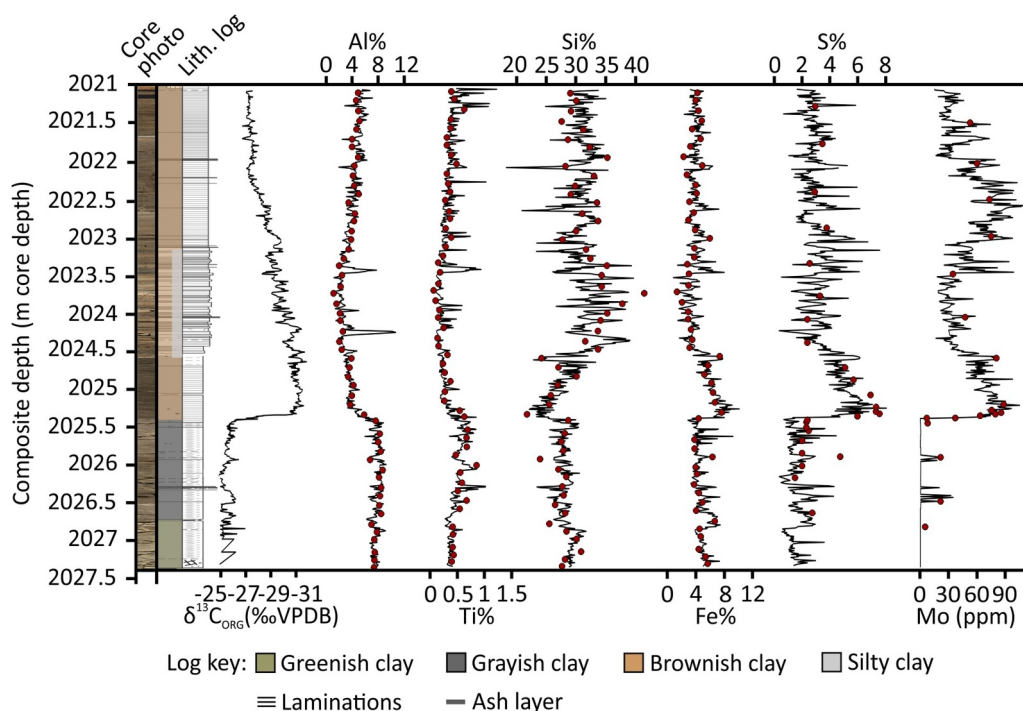
Figure 2. E−8X lithological log, $\delta^{13}C_{org}$ and elemental analysis. Black curves represent data acquired with pXRF (adjusted using bXRF for Al, Si, and Mo, see Section 2), red dots correspond to datapoints collected with bXRF and $^{100}Mo/^{95}Mo$.

determined by Stokes' Law, after which the "clay" (<4 μm) and "silt" (4–63 μm) fractions were dried at 55°C and stored in glass vials. Although clays are classified as <2 μm particles, a larger particle diameter (i.e., <4 μm) is preferred in smectite-rich sediments (Kemp et al., 2016). The production of oriented mounts, as well as XRD analysis and data modeling followed the methods outlined by Kemp et al. (2016).

3. Results and Discussion

3.1. Development of Euxinia During the PETM

Terrigenous elements Al and Ti display their highest relative abundance values during the pre-PETM interval, followed by a decrease coinciding with the CIE onset (∼2,025.4 m; Figure 2). The relative abundances slightly increase during the recovery phases (∼2,023–2,021 m), but do not reach pre-PETM values. Si, like Al and Ti, is present in the aluminosilicate phase although it can also originate from quartz silts and sands, and biogenic silica. During the pre-PETM, Si is constantly around 30% followed by a decrease of ∼5% at the CIE onset (∼2,025.4 m; Figure 2). The highest relative abundance values coincide with the silty interval observed between 2,024.5 and 2,023.1 m (Figure 2).

Iron relative abundance remains overall constant throughout the interval with the exception of an increase at the CIE onset (∼2,025.4 m) and the main phase between 2,025.4 and 2,024.5 m (Figure 2). Sulfur exhibits its lowest values of the entire record during the pre-PETM, followed by a major increase at the CIE onset (∼2,025.4 m), and by a decrease in the lower part of the main phase (∼2,025.2 m–∼2,024.3 m). Sulfur gradually decreases throughout the recovery phases, reaching lowest levels during recovery Phase 2 when compared to recovery Phase 1 and main phase, albeit not declining to pre PETM levels (2,022–2,021 m; Figure 2). The sharp increase of S at the CIE onset may suggest incorporation under reducing conditions (Croudace & Rothwell, 2015; Sluijs et al., 2008; Figure 2).

Major and trace elements are normalized against Al and Ti to account for the dilution effects of terrestrial sediment input rate (Tribovillard et al., 2006). The most significant geochemical changes in core E−8X are observed at the CIE onset (∼2,025.4 m, Figures 2 and 3) where all redox proxies point to a shift from oxic/suboxic
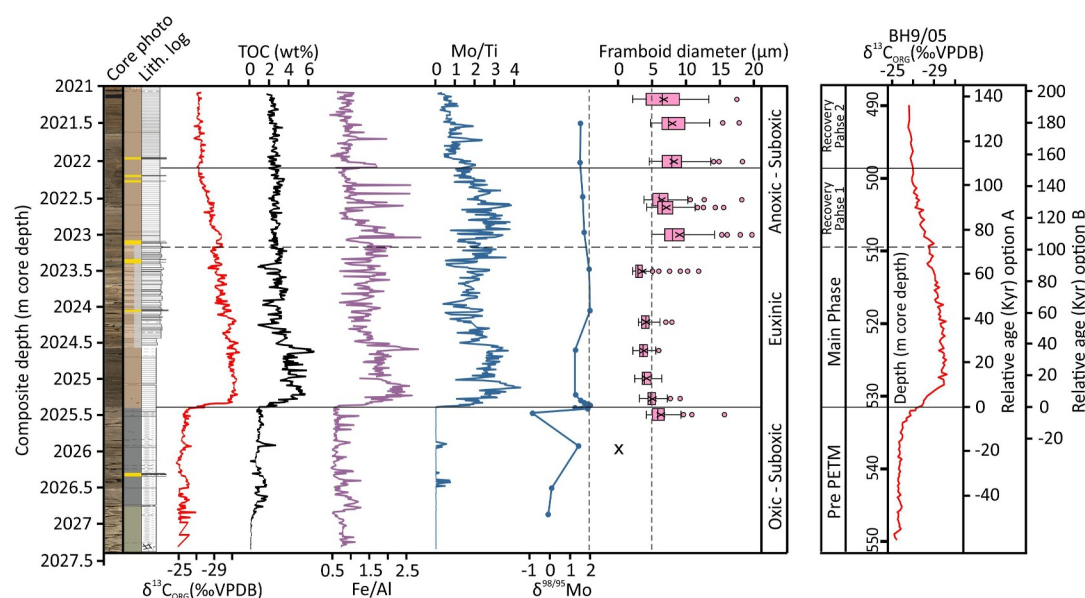
Figure 3. Data from pXRF, Mo isotopes and pyrite framboids from core E−8X. Core photos and simplified lithological log are from Kender et al. (2021). The $\delta^{13}C_{org}$ and TOC (wt%) values presented herein are a compilation of data from this study and previous measurements from Kender et al. (2021). The box and whisker plots of framboid size consist of first quartile (25th percentile) and third quartile (75th percentile). The vertical line within each box is the median value, and the X represents the average value. Whiskers symbolize minimum and maximum values, excluding outliers (individual dots). Outliers are identified through the 1.5 interquartile range rule. The dashed blue line indicates the maximum average diameter for syngenetically formed framboids. An additional dashed blue line along the Mo isotope curve indicates a $\delta^{98/95}Mo$ value of ~1.94‰, corresponding to the peak values observed in Site M0004 A (Arctic Ocean) and interpreted as global paleo-sea water isotopic composition (Dickson et al., 2012). The age model shows 'option A and B' from core BH9/05 (Charles et al., 2011) (see Kender et al., 2021).

to anoxic/euxinic bottom water settings. For instance, the Fe/Al increase at the CIE onset (Figure 3) suggests that a portion of Fe is present in pyrite rather than in detrital material (Lyons & Severmann, 2006).

Aqueous Mo, another diagnostic redox-sensitive proxy, is abundant in modern oxygenated marine basins where it is unreactive (Algeo & Lyons, 2006). However, under anoxic conditions Mo is transferred into the sediment (Helz et al., 1996, 2011; Supplementary Material). The rapid increase in Mo/Ti at the early onset of the PETM CIE is characteristic/diagnostic of a fast transition to euxinic settings (Figure 3). Molybdenum isotope ratios ($\delta^{98/95}Mo$) have been applied as a seawater redox proxy during the PETM in the Arctic and Tethys Oceans (Dickson et al., 2012; Dickson, Cohen, & Coe, 2014; in Supporting Information S1), as ^{95}Mo is preferentially removed during Mo absorption onto Mn oxides in oxic settings, which are fractionated from seawater by −3‰ (Dickson, 2017). Anoxic environments of intermediate reducing conditions, with $H_2S < 11$ µmol l^{-1}, display a near constant seawater isotopic fractionation of ~0.7‰ due to non-quantitative Mo drawdown (Dickson, 2017). When $H_2S > 11$ µmol l^{-1}, a geochemical switch point is activated under which Mo exists as tetrathiomolybdate and can be removed from the water column (quantitative Mo drawdown), yielding low seawater isotopic fractionations of 0.5‰ (Dickson, 2017). The shift from light (0.11‰ to −0.84‰) to heavy (1.27–1.99‰) sediment $\delta^{98/95}Mo$ isotopic composition in E−8X indicates broadly oxic conditions before the PETM (note a temporary shift to heavy values at 2025.93 m where the sediment becomes briefly laminated and enriched in TOC; Figure 3) that rapidly changed to sulfidic conditions at the CIE. The first half of the main phase, between ~2025.2 m and ~2024.5 m, records a slight return to lighter $\delta^{98/95}Mo$ values. The second half of the main phase between ~2024.5 m and ~2023.2 m is characterized by heavy values around 2‰. Although a slight decrease is observed throughout the recovery phases, $\delta^{98/95}Mo$ values remain above 1‰.

Pyrite framboid diameters have also been used as a proxy for redox conditions (Bond & Wignall, 2010; Wilkin et al., 1997). Pyrite framboids form via two pathways based on bottom water oxygen levels, with mean diameters between 3 and 5 µm occurring in euxinic settings, and larger diameters up to 50 µm typical of suboxic conditions (Wilkin et al., 1997; Bond & Wignall, 2010; in Supporting Information S1). The pyrite framboid size distribution
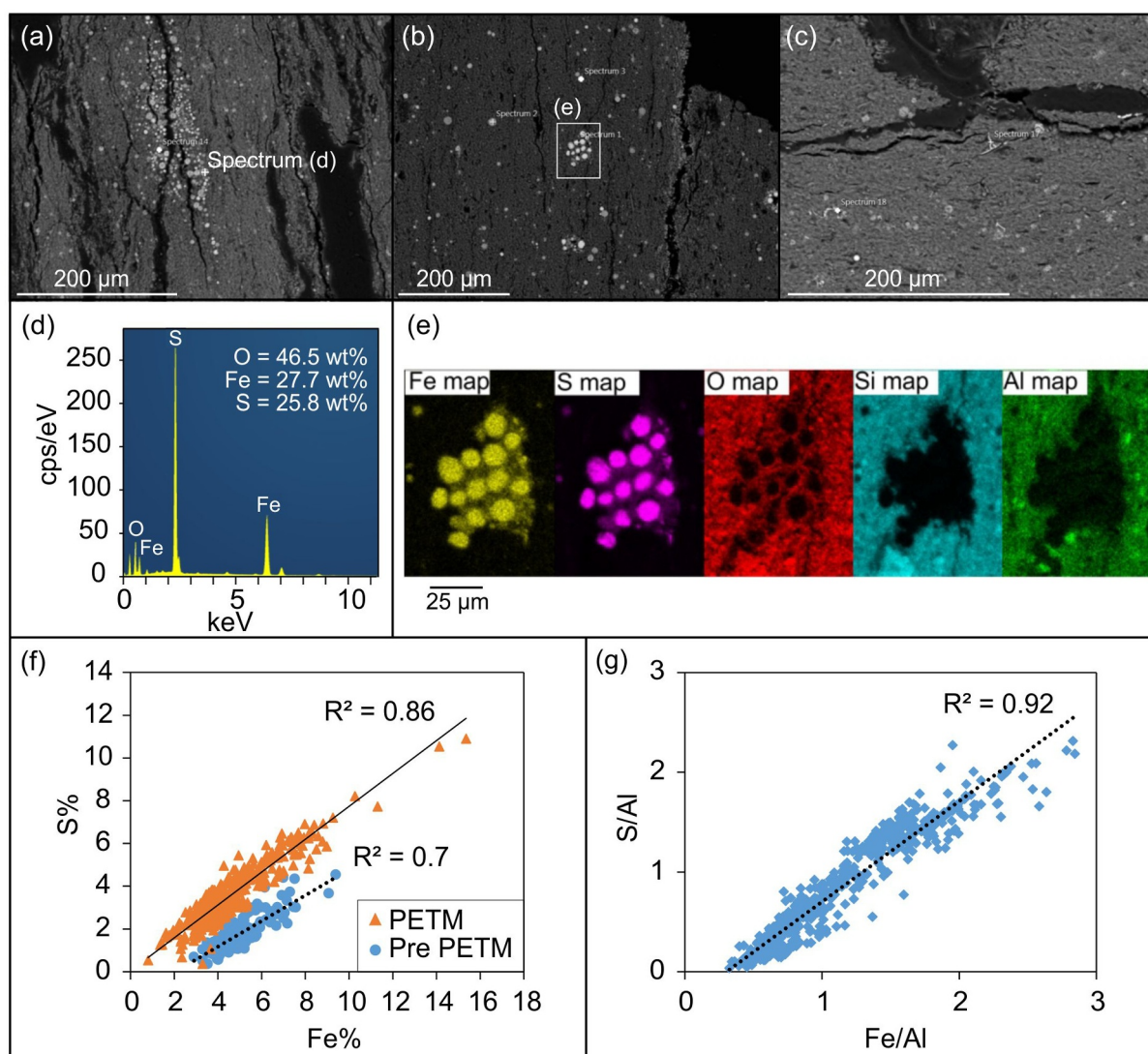
Figure 4. Pyrite framboid images, spectral analysis, elemental maps and cross plots. (a) Main phase sample (MPA 63928, 2025.05 m) displaying numerous packed framboids. (b) Recovery Phase 1 sample (MPA 66450, 2022.51 m) showing isolated and, occasionally, clustered framboids. (c) Recovery Phase 2 sample (MPA 66351, 2021.5 m) with rare framboids and pyritized silicofossil fragments. (d) Spectral analysis of framboids in the main phase sample (spectrum d in a). (e) Elemental mapping of framboid clusters in the recovery Phase 1 sample (cluster 'e' in b), clearly showing pyrite framboids in a clay-dominated matrix. (f) Handheld XRF Fe% versus S%. (g) Handheld XRF Fe/Al versus S/Al.

at the CIE onset supports syngenetic growth under euxinic conditions (Figures 3 and 4a). No pyrite framboids are observed under the scanning electron microscope in the sample at ~2026 m and the pre PETM interval in general contains much lower pyrite abundance as inferred from low S% and Fe/Al (Figures 2 and 3). Framboids are observed just prior to the CIE onset (2025.5 m, Figure 3), yielding a wide range of sizes and an average diameter of ~6 µm indicating suboxic conditions. Larger pyrite framboids are present throughout the recovery phase intervals, where diameters reach up to 20 µm, typical of anoxic/suboxic environments (Figures 3 and 4b, c). The framboids become more sporadic at the recovery Phase 2, suggesting an attenuation of anoxia (Figures 4b and 4c).

The presence of pyrite is further corroborated by the positive correlation between Fe% and S%, whereas the strong positive correlation between Fe/Al and S/Al suggests that some of Fe and S is bound to the clay source (Figures 4f and 4g).

To summarize, the pre-PETM is characterized by predominantly weakly laminated sediments, low pyrite (S and Fe) and Mo abundances generally below the limit of detection (Figure 2). We interpret these proxy patterns (lack
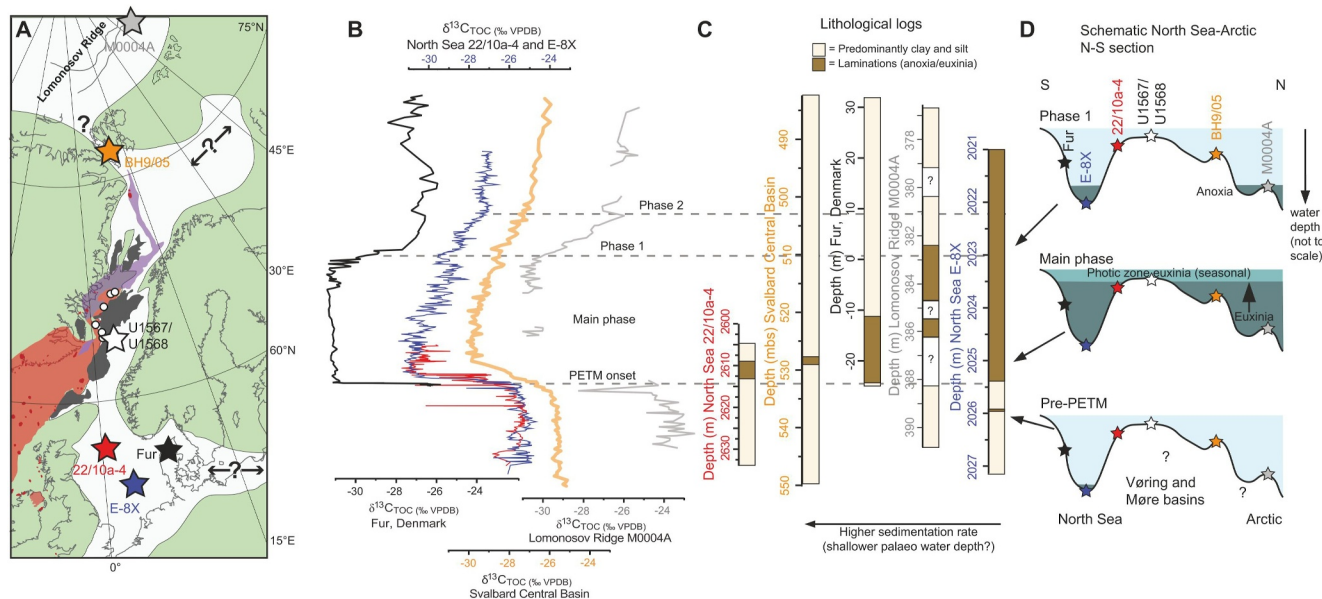
Figure 5. Comparison of PETM sites across the North Sea, Norwegian Sea and Arctic. (a) Map showing the location of North Sea sites (22/10a-4, E−8X and Fur), IODP 396, Spitsbergen section BH9/05 and Lomonosov Ridge site M0004 A. Figure adapted from Jones et al. (2023), with Arctic Ocean reconstruction based on Golonka (2009). (b) δ¹³C curves from Fur (black line), E−8X (blue line), 22/10a-4 (red line), BH9/05 (orange line) and M0004 A (gray line). (c) Simplified lithological logs of PETM sites showing onset of laminations around the CIE. (d) Schematic North Sea and Arctic N-S section showing changes in redox conditions as a function of water depth across the North Sea, Norwegian Sea and the Arctic.

of clearly laminated sediments, low pyrite content and no appreciable Mo concentrations) typical of oxygenated bottom water conditions. Short suboxic episodes appear to have occurred, consistent with the observation of occasional laminations, high Mo abundance horizons (up to 20 ppm, concentrations significantly above crustal values), and framboid sizes typical of suboxic conditions (Figures 2 and 3). Unlike the pre-PETM, the CIE onset and PETM main phase record continuous sediment lamination, high pyrite (Fe and S), small diameter pyrite framboids (<5 μm), rapid increase in Mo abundance and heavier Mo isotopes, typical of euxinic conditions and significant trace metal depletion (Figures 2 and 3). This profound redox transition is consistent with previous observations from Fur Island (Figure 1), and Arctic Ocean Site M0004 A, where laminated sediment and S-bound isorenieratane presence is indicative of photic zone euxinia (Schoon et al., 2015; Sluijs et al., 2006; Stokke et al., 2021).

Comparison of PETM sites across the North Sea-Norwegian Sea-Arctic Ocean (Figure 5) shows that laminated sedimentation appeared approximately simultaneously at the onset of the PETM across the region, which may be indicative of anoxia/euxinia as we have found for E−8X. Laminated sediments at the PETM onset are reported from Fur Island, Denmark (Jones, Percival, et al., 2019), which is closest to our site. In addition, recent sites U1567 and U1568, a collection of five holes from International Ocean Discovery Program (IODP) Expedition 396 (Planke et al., 2023) forming a transect across the Modgunn hydrothermal vent complex (HTVC) in the Møre Basin, all show a change to laminated mudstone coeval with the onset of the PETM (Berndt et al., 2023). However, sites reverted to unlaminated sedimentation at varying times within the main and recovery phases. This may have been driven predominantly by a shrinking oxygen minimum zone (OMZ) and expanding mixed depth that caused shallower sites to become oxic before deeper sites. Although we cannot accurately reconstruct paleo water depth, the sites with lower sedimentation rates appear to retain laminations for a longer period of time (e.g., E−8X) which may indicate that deeper sites were affected by anoxia/euxinia for longer as sedimentation rates tend to be highest in shallow and nearshore settings (e.g., Svalbard site BH9/05, where palynology interpretations indicate marginal marine conditions, Harding et al., 2011; Fur, which has been interpreted as outer neritic, Schoon et al., 2015). Although we are unable to correlate Sites U1567 and U1568 with the other records in Figure 5 as the CIEs are of slightly lower resolution in places (Berndt et al., 2023), we do note that these sites revert to unlaminated sedimentation during the PETM main phase which is consistent with their interpreted shallow marine water depth (Berndt et al., 2023). By contrast, the rapid infill of the Modgunn hydrothermal vent complex on the
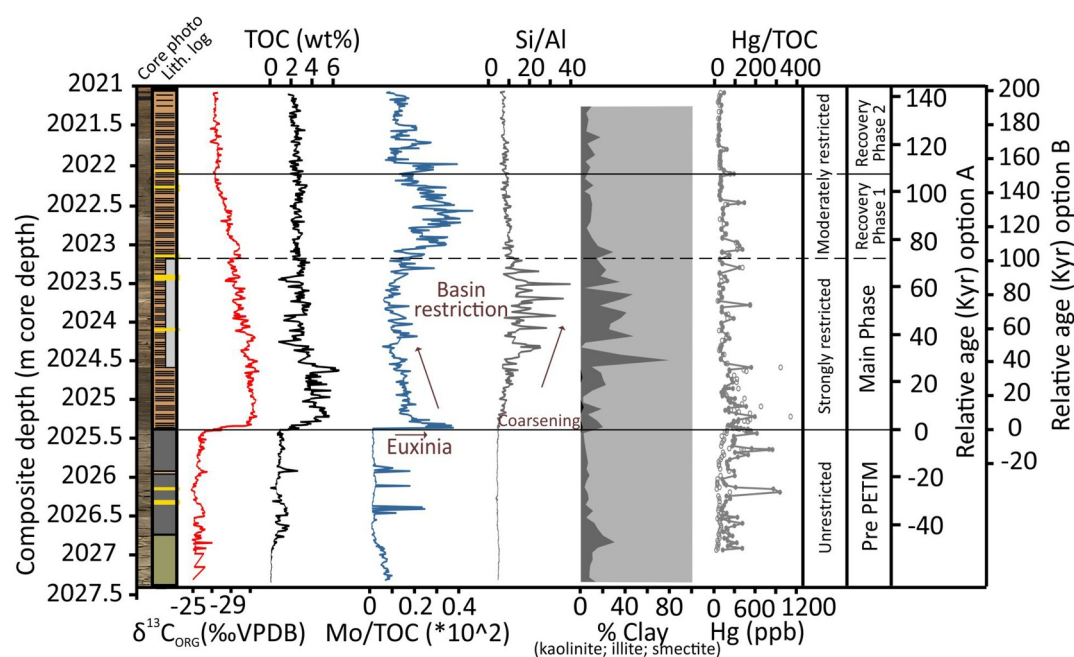
Figure 6. $\delta^{13}C_{org}$, TOC (wt%), Mo/TOC, Si/Al ratio and clay minerals of core E−8X. The TOC (wt%) from Kender et al. (2021) indicates relative changes in productivity and Mo/TOC as a basin restriction proxy. Si/Al and clay mineralogy are used to show the influence of coarse and fine-grained sediments, respectively. Mercury data from Kender et al. (2021). The age model option A and B are from Charles et al. (2011) (see Kender et al., 2021).

Norwegian continental margin means that the water depth of the lowermost-PETM strata may be considerably greater than at the top of the vent infill, which is still within the PETM, because Hole U1568A contains ∼80 m of syn-PETM infill (Berndt et al., 2023). Therefore, the potential effect of water depth on recording anoxia may be affected by the rapid infill of the vent crater that was initiated as a significant bathymetric depression. Our interpretation of a rapid onset of regional euxinia at the PETM onset, followed by gradually contracting OMZ and expansion of the mixed layer (perhaps via reduced salinity stratification: Zacke et al., 2009; Kender et al., 2012), suggests the North Sea–Norwegian Sea–Arctic basins were highly tectonically restricted and sensitive to further tectonic uplift and hydroclimate-driven productivity changes.

3.2. Basin Restriction and NAIP Emplacement

Our Mo/TOC data provides evidence for basin restriction of the North Sea over the PETM (Figure 6). It has been shown that in silled basins the limited aqueous Mo availability results in reduced sedimentary burial of Mo per unit of organic matter (the 'basin reservoir effect'; Algeo & Lyons, 2006; in Supporting Information S1), and consequently the Mo/TOC ratio can be used as a basin restriction proxy. Mo/TOC values in E−8X are highest (∼0.4×10^2) during the CIE onset (∼2025.4 m) and gradually decrease throughout the main phase of the PETM to values between 0.05 and 0.15 (Figure 6). We suggest that the high Mo/TOC values at the CIE onset resulted from the initial drawdown of aqueous Mo from the previously less restricted North Sea basin. Similar behavior has been observed at the start of Ocean Anoxic Event (OAE) two in the hydrographically restricted Proto-North Atlantic Ocean (Owens et al., 2016). Mo/TOC values in core E−8X remain low for the main phase of the PETM consistent with a strongly restricted basin with deep water renewal times >500 years (Algeo & Lyons, 2006). This is further supported by Osmium (Os) isotope records from nearby Fur Island pointing to strong basin restriction during the PETM (Jones et al., 2023).

Additional evidence of basin restriction during the PETM is found in the E−8X $\delta^{98/95}$Mo isotopic signature: assuming global seawater composition of ∼1.95‰ for the PETM (Dickson et al., 2012), the E−8X $\delta^{98/95}$Mo values of ∼2‰ during the main phase (Figure 3) are similar to Arctic Ocean marine sediments (Dickson et al., 2012). Such heavy isotopic values are achieved under quantitative Mo drawdown in euxinic conditions, which result in direct capture of seawater isotopic composition. However, quantitative Mo removal in euxinic

settings can be hindered if exchange with open ocean water is high. Consequently, sedimentary $\delta^{98/95}$Mo approaching the global ocean value is usually associated with euxinic and restricted basins (Dickson, 2017). As E−8X Mo isotope values are similar to those observed in the Arctic Ocean (Dickson et al., 2012), we use these to interpret comparable depositional conditions, characterized by euxinia and trace metal drawdown under strong hydrographic restriction. Box modeling has been carried out on the fractional removal of Mo in euxinic sediments as a function of the isotopic composition of modern, PETM, OAE 2, and Toarcian-OAE seawater and a steady riverine input (Dickson, 2017). According to the model, lower seawater Mo isotope compositions require higher removal of Mo into sediments, and therefore a larger extent of seafloor euxinia compared to the present.

We suggest that the North Sea basin restriction during the PETM was caused by NAIP emplacement. Several lines of evidence support regional uplift and relative sea level fall associated with NAIP emplacement, including lithostratigraphy and seismic stratigraphy of Paleocene–Eocene successions around the North Sea (Hartley et al., 2011; Maclennan & Jones, 2006; Svensen et al., 2004). The uplift was primarily caused by pulsating upward flow of the Icelandic mantle plume between Greenland and Scotland, which spread outwards beneath the NW continental margin (Hartley et al., 2011; Jones, Hoggett, et al., 2019; Figure 1). It is important to note that sedimentary Hg and Hg/TOC values in E−8X and nearby cores 22/10a-4 (Kender et al., 2021) and 23/16b-9 (Jin et al., 2023), in addition to Hg records from Fur and Svalbard (Jones et al., 2019a, 2023), indicate that volcanic activity was enhanced in the lead up to and during the CIE onset (Figure 6), suggesting a direct and causal association of NAIP volcanism and the PETM. Additional sedimentary Hg enrichments coinciding with the PETM have been documented from other study areas globally and have been related to NAIP volcanic activity (Liu et al., 2019; Tremblin et al., 2022). Thousands of intruded sills have been recognised in 2D and 3D seismic reflection profiles between the Faroe-Shetland basin (offshore NW Scotland) and the Vøring and Møre basins (Norwegian Sea), with up to 400 m thickness (Berndt et al., 2023; Jones, Percival, et al., 2019; Svensen et al., 2004). Although the vertical displacement and uplift rates are yet to be constrained, we hypothesize that the thick NAIP sills, which may have been emplaced rapidly (possibly down to a few years, Jones, Percival, et al., 2019), must have had a significant topographic impact on the northwestern North Sea basin and on the northern North Atlantic region. Further evidence of a shallow and restricted northern North Atlantic comes from IODP Sites U1567 and U1568, where five holes through the Modgunn hydrothermal vent complex were drilled, and 3D seismic mapping was performed. The results suggest that the Modgunn vent complex formed a few thousand years before the PETM onset under shallow marine waters, whereas other hydrothermal vent complexes in the Modgunn Arch might have developed under short-lived subaerial settings (Berndt et al., 2023), supporting the assumption that the proto-Northeast Atlantic was possibly very susceptible to topographic changes. The interpretation of sedimentological, palynological and 2D seismic stratigraphic data propose that a complex fragmentation of both the northeastern North Atlantic (Norway-Greenland seaway) and the western North Atlantic (Greenland-Scotland Ridge) occurred at the Paleocene-Eocene, as a result of regional tectonic uplift (Hovikoski et al., 2021).

Basin restriction via uplift and relative sea level fall may explain our Si/Al and clay mineralogy data (Figure 6). High Si/Al values in E−8X could reflect biogenic silica from diatoms, and/or quartz content in the silty interval as observed in the fine fraction XRD analysis. During the main phase the clay assemblage exhibits higher illite within a smectite-dominated background, and trace occurrence of kaolinite (Figure 6). Kaolinite is composed of coarser grains, with illite and then smectite composed of progressively finer grain sizes. In the Paleogene North Sea basin, high abundances of kaolinite and illite at the basin margins and a high abundance of smectite in the central area were interpreted as a consequence of current sorting during transport (Nielsen et al., 2015; Supplementary Material). Sediment size coarsening during the main phase is supported by increased illite content versus smectite and peaks of Si/Al in the silty interval between 2,024.5 and 2,023.2 m (Figure 6). We argue that local relative sea level fall from tectonic uplift could have shifted the paleo shorelines making E−8X closer to continental sediment sources, where coarser particles reached the site. Alternatively, increased grain size may reflect an increased flux of terrigenous material, as suggested by lithium isotope excursion records at the PETM onset interpreted to be a response to enhanced hydrological cycle due to global warming (Pogge von Stradmann et al., 2021; Jones et al., 2023).

3.3. Precursor Signals and an NAIP Trigger for the PETM

The PETM was a complex event: in addition to global temperature increase (Dunkley Jones et al., 2013), some sea surface temperature and continental proxies hint to a transient warming prior to the CIE onset (Secord et al., 2010;
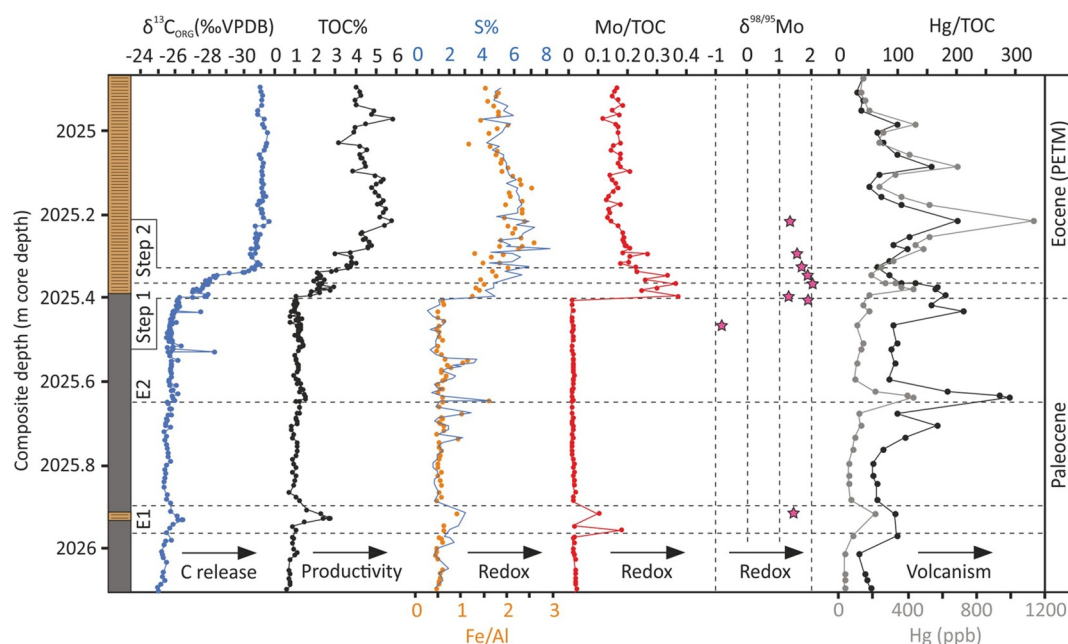
Figure 7. Carbon release, productivity, redox and volcanic proxies in core E−8X. Precursor events E1 and E2, and the two-step CIE are shown.

Sluijs et al., 2007), while marine environments display highly variable regional and local water column salinity and stratification (Sluijs & Brinkhuis, 2009). Areas proximal to the NAIP emplacement area, such as the North Sea, may have faced far more direct and local consequences to the tectonic uplift and sill intrusions, such as precursor cooling from volcanic SO_2 injections (Stokke et al., 2021), which are not observed in other distal locations globally. Alternatively, the tectonic uplift resulting from NAIP emplacement might have caused an episodic cooling event by modifying the positioning of the Northern Hemisphere jet stream (Vickers et al., 2024). These proximal areas may therefore hold the key to separate trigger and response during the initial onset of the CIE, specifically the role of volcanic uplift and emissions as causal triggers for the development of environmental change during the PETM main phase. The North Sea–Norwegian Sea–Arctic Ocean were restricted with a strong low salinity halocline in place (Harding et al., 2011; Kender et al., 2012; Zacke et al., 2009), and the OMZ would have been sensitive to changes in tectonic restriction, and riverine influxes of nutrients causing plankton blooms perhaps in some ways similar to the modern Black Sea (Bologa et al., 1999). Plankton blooms during the PETM have been documented in the northwestern North Sea (Eldrett et al., 2014; Kender et al., 2012) and offshore the Møre Basin, Norway (Berndt et al., 2023).

Before the PETM, in E−8X a stratigraphically short occurrence of laminated sedimentation (~2,025.94 m; marked as "E1" in Figure 7) occurred with increased Mo, pyrite (S and Fe), $\delta^{98/95}$Mo, TOC and negative δ^{13}C. This indicates a brief period of anoxia/euxinia driven by elevated productivity (TOC), which may be linked to volcanism as there is a coeval increase in Hg/TOC. Event E1 is unlikely to have been caused directly by basin restriction from NAIP uplift, as its short-lived nature would imply rapid subsequent tectonic relaxation and subsidence in contrast to evidence for gradually increasing sill emplacement and volcanic intensity (Berndt et al., 2023; Jones, Hoggett, et al., 2019; Kender et al., 2021). We speculate that volcanic activity releasing Hg and carbon (negative δ^{13}C spike) caused oceanographic change which translated into eutrophication of the North Sea. This event may also be expressed in 22/10a-4 (Kender et al., 2012) where there are short-lived precursor δ^{13}C spikes associated with eutrophication, but it has not been detected outside the North Sea region although we note it is short-lived and could have been missed at sites with lower sampling resolution.

We suggest that this apparently local (to the North Sea) precursor eutrophication E1 signal was unlikely the result of massive greenhouse gas release causing global warming and an increased hydrological cycle (as suggested for the PETM). One line of evidence comes from terrestrial palynological data around the North Sea, which are inconsistent with pre-PETM warming and rather depict a vegetation dominated by temperate conifers up to the

CIE onset (Collinson et al., 2009; Kender et al., 2012; Lenz & Riegel, 2001). Conversely, the CIE onset is associated with data pointing to climatic perturbations possibly due to the carbon input: higher plant biomarkers and their hydrogen isotopic composition at Vasterival, Southern North Sea, suggest a shift from dryer to moister conditions due to increased meteoric water input at the CIE onset (Garel et al., 2013). A change from dry to warmer and wetter conditions at the CIE onset is also reconstructed from carbon isotopes of the biomarker hopanoids at Cobham, Southern North Sea (Pancost et al., 2007). Likewise, Cobham palynological data records a shift from dry fire-prone pre-PETM vegetation to wetter conditions and decreased fire regime during the PETM (Collinson et al., 2009), suggesting a profound climatic change consistent with the CIE onset. As an increase of Hg/TOC is consistent with event E1 (Figure 7), and given the paucity of evidence suggesting major climate changes during the pre-PETM interval, we argue that E1 was rather controlled by volcanic NAIP-related phenomena perhaps from atmospheric S and ash affecting regional rainfall and riverine discharge, and/or nutrient delivery from massive hydrothermal venting directly into ocean water (Svensen et al., 2004). A subsequent possible PETM precursor event occurs in E−8X (~2,025.65 m; "E2" in Figure 7), which is similar to E1 (negative δ^{13}C spike, TOC and pyrite increase) but smaller and with no increase in Mo, is associated with increased Hg/TOC and may have had similar causal mechanisms. Alternatively, increased productivity during E1 and E2 may have been the result of Milankovitch-forced local insolation and rainfall-related changes interacting with a basin close to a tipping point, with the Hg increases being coincidental. Either way, the presence of E1 and E2 indicate that the North Sea basin had already become restricted by uplift from previous activity of the NAIP (evidenced by precursor Hg spikes, Kender et al., 2021; geochronological constrains of ash layers and volcanic sequences across Greenland, Faeroe Islands, UK, and Norway predating the PETM onset; Storey et al., 2007; Wilkinson et al., 2017), such that an ephemeral increase in productivity was able to cause OMZ expansion and euxinia.

Further evidence for basin restriction prior to the PETM comes from the Northern North Sea, where at site 22/10a-4 low salinity/eutrophic dinoflagellate cysts gradually increase in proportion suggesting early oceanic eutrophication from enhanced productivity (Kender et al., 2012). As we find no early long-term increase in productivity (TOC) in the Southern North Sea (E−8X), we proposed the 22/10a-4 signal was related to continued uplift of the NAIP causing local increases in riverine runoff perhaps from an uplifted Faeroe–Shetland platform (Kender et al., 2012). There is no evidence for increased warming prior to the PETM in the North Sea basin as a mechanism to force such a change; instead, sea surface temperature proxy data indicates a possible cooling episode, although this is complicated by high BIT index values and associated uncertainties of interpreting the data (Schoon et al., 2015; Stokke et al., 2020).

At the onset of the PETM (CIE step 1; Figure 7) we observe elevated $\delta^{98/95}$Mo, pyrite and Mo/TOC, whereas the increase in TOC lags $\delta^{98/95}$Mo, pyrite and Mo/TOC by one sample, corresponding to ~300 years time step according to our sample resolution and simple age model (Figure 3; Kender et al., 2021), again occurring with elevated Hg/TOC. Although this apparent time lag could be explained by further tectonic uplift and restriction of the North Sea causing euxinia before any major climate-driven eutrophication, it is possible that the onset of bottom water euxinia changed pore water redox chemistry several cm below the sea floor. Therefore, it is consistent that enhanced productivity forced the early OMZ expansion (as in precursor events E1 and E2) either by global climate change at the PETM onset, or more likely local eutrophication from volcanic processes as in the precursor events given this change was so early at the CIE onset. CIE step 2 corresponds to a further release of CO_2 that may have been triggered from initial volcanism, and the pulsed increases in TOC suggest global warming and increased global hydrological cycling was continuing to more heavily impact the productivity regime in the North Sea (Figure 7).

3.4. Recovery From the PETM

A partial attenuation of both basin restriction (Mo/TOC) and euxinia (S, Fe/Al, and pyrite framboid size) is observed from the base of recovery Phase 1, ~70 kyr after the main carbon isotope excursion (Figures 3 and 6). A decrease of S and Fe/Al compared to main phase values suggests anoxia-suboxia, in contrast to the high Mo and Mo/Ti values typical of persistent euxinia. We interpret this discrepancy during recovery Phase 1 as Mo/TOC values indicating a shift from strong to moderate basin restriction, which would have allowed at least partial renewal of aqueous Mo. Thus, we suggest that high Mo and Mo/Ti values in recovery Phase 1 are, for the most part, a result of Mo renewal rather than a response to changing redox conditions. Mo renewal could have been caused by tectonic relaxation and minor subsidence, and/or sea level rise from climatic changes and ocean warming. Sulfidic conditions likely still existed at this time, as supported by high $\delta^{98/95}$Mo, but were located

closer to the seafloor given the increase in pyrite framboid size distributions that indicate dominantly authigenic rather than syngenetic processes.

Both Mo and Mo/Ti indicate anoxic-suboxic conditions during the recovery Phase 2, a paleoenvironmental setting which is supported by the pyrite framboid size distribution. We suggest that at this time, the Mo/TOC signal loses its reliability because the proxy is applicable only to systems where at least weakly sulfidic conditions existed (Algeo & Lyons, 2006). The gradual decrease in $\delta^{98/95}$Mo values during both recovery phases may represent a gradual deepened chemocline either following partial opening of the North Sea basin, and/or reduced primary productivity due to partial climate recovery, combined with overall lower H_2S availability (Figure 3). Relatively high Mo concentrations throughout the recovery phases, however, suggest that H_2S was still present at the local sediment-water interface.

Weakened basin restriction (rising Mo/TOC values) and a decrease in coarser sediment (low Si/Al values, a return to pre PETM proportions of illite and smectite) is consistent with a relative sea level rise (tectonic and/or climate driven), defining the local response of the North Sea region to the recovery Phase 1 of the PETM. In the North Sea, anoxic-suboxic bottom water conditions persisted throughout the recovery phases at E−8X despite possible sea level rise. We speculate this could be related to the slow (Myr) NAIP subsidence from waning effects of thermal uplift (Hartley et al., 2011) which kept the North Sea moderately restricted for large parts of the recovery phases with intermittent anoxic-suboxic periods, and the gradual reduction in the extent of the OMZ affecting deeper sites for longer (Figure 5). It is important to note that our suggested hypothesis of partial attenuation of basin restriction during the recovery phases is somewhat in contrast with other sites in the North Sea. Osmium isotope records (^{187}Os/^{188}Os) from Fur Island indicate a strong deviation from the global ocean signal coinciding with the start of the recovery phase, suggesting that the North Sea became restricted after the hyperthermal event (Jones et al., 2023). However, the Os isotopic shift at the end of the PETM correlates with a variation in lithium isotopes (δ^7Li), a proxy for siliciclastic input and erosion of ash deposits. This suggests an increase in basalt-derived fluxes during the recovery phase, and if these fluxes have different Os isotopic signatures, then the reliability of ^{187}Os/^{188}Os as a proxy for water connectivity might be hindered. Although quantifying the extent of basin restriction relaxation during the recovery phases is beyond the scope of this study, it is important to note that restriction changes might have been more subtle than our proposed shift from 'strongly restricted' to 'moderately restricted' North Sea after the PETM main phase. This would be more aligned with salinity records (Zacke et al., 2009) and uplift reconstructions (Conway-Jones & White, 2022) that suggest the North Sea remained somewhat restricted during the early Ypresian.

In core E−8X, the main phase and recovery phases may cover a time span of ~140 kyr. According to our data, the bottom water environment responded close to instantaneously (~300 years) to the hydrographic restriction threshold, and never fully recovered to pre PETM oxic conditions for at least ~140 kyr. Sustained anoxic conditions are prone to carbon burial and when coupled with increased silicate weathering, required to resolve the short duration of the PETM recovery (Penman & Zachos, 2018), our data support that North Sea and nearby basins could have been important carbon sinks throughout the observed interval (Papadomanolaki et al., 2022; Stokke et al., 2021). Future modelling studies will allow assessment of the role this local and relatively small carbon sink played as part of the global PETM perturbation.

4. Conclusions

New high-resolution geochemical data from exceptionally well-preserved marine sediment core E−8X are used to reconstruct hydrography and bottom water conditions during the PETM in the North Sea basin. Bottom water oxygen depletion is commonly associated with climatic responses to atmospheric warming, such as increased hydrological cycling, water column stratification, and eutrophication due to increased nutrient input. However, we find that North Sea redox, productivity and basin restriction changes occurred before the major carbon injection and global strong climatic changes associate with the PETM. Short-lived precursor PETM events (E1 and E2) co-occur with low δ^{13}C, high productivity, low oxygen and volcanic pulses (Hg/TOC), evidencing a tectonically restricted basin where Large Igneous Province (LIP)-related activity caused eutrophication, forcing the North Sea past a tipping point toward oceanic anoxia. This could be related to atmospheric ash and S releases causing local changes in hydrology, river runoff and nutrient discharge, and/or hydrothermal venting injecting nutrients along with Hg directly into the North Sea. A similar scenario is interpreted for the PETM onset where rapid early eutrophication and euxinia demonstrate LIP activity control over North Sea oceanography before the

largest global warming and climatic changes occurred. Rapidly declining Mo/TOC with continued high $\delta^{98/95}$Mo in the main phase of the PETM further evidences a restricted basin associated with activity of the NAIP. Early PETM recovery is associated with a slightly less restricted North Sea Basin, which could have been due to minor tectonic subsidence after the NAIP uplift associated with the PETM onset, and/or sea level rise driven by climatic changes and ocean warming. Nevertheless, persistent high productivity and low oxygen throughout our records show the North Sea Basin never fully recovered to pre PETM oxic conditions for at least ∼140 kyr.

Our findings suggest LIP emplacements should not be disregarded as a driver of significant biogeochemical changes at time scales similar to modern climatic change, although limited to a regional scale and proximal localities. The timing and lead-lags between carbon injection, eutrophication and basin restriction provide further evidence that NAIP activity was a causal trigger for the carbon cycle disruption. This fine temporal separation of geochemical proxy evidence for volcanic versus climatic mechanisms, combined with the pulsed nature of NAIP volcanism, demonstrates that deep mantle dynamics related to LIP emplacements can, at least locally, result in strong ocean biogeochemical feedbacks, at time scales commonly associated with climatic response. This concept can be tested for other LIP-shelf sea regions to understand the cascade of trigger–response mechanisms that may lead to global hyperthermal events, or failed events.

Data Availability Statement

Data files are publicly available at PANGAEA – Data Publisher for Earth & Environmental Science (Mariani et al., 2024).

References

Algeo, T. J., & Lyons, T. W. (2006). Mo–total organic carbon covariation in modern anoxic marine environments: Implications for analysis of paleoredox and paleohydrographic conditions. *Paleoceanography*, *21*(1), PA1016. https://doi.org/10.1029/2004PA001112

Berndt, C., Planke, S., Alvarez Zarikian, C. A., Frieling, J., Jones, M. T., Millett, J. M., et al. (2023). Shallow-water hydrothermal venting linked to the Palaeocene-eocene thermal maximum. *Nature Geoscience*, *16*(9), 803–809. https://doi.org/10.1038/s41561-023-01246-8

Bologa, A. S., Frangopol, P. T., Vedernikov, V. I., Stelmakh, L. V., Yunev, O. A., Yilmaz, A., & Ogun, T. (1999). Distribution of planktonic primary production in the Black Sea. In S. T. Beşiktepe, Ü. Ünlüata, & A. S. Bologa (Eds.), *Environmental degradation of the Black Sea: Challenges and remedies*, *NATO Science Series* (Vol. 56, pp. 131–145). Springer. https://doi.org/10.1007/978-94-011-4568-8_9

Bond, D. P. G., & Wignall, P. B. (2010). Pyrite framboid study of marine Permian-Triassic boundary sections: A complex anoxic event and its relationship to contemporaneous mass extinction. *Geological Society of America Bulletin*, *122*(7–8), 1265–1279. https://doi.org/10.1130/B30042.1

Carmichael, M. J., Inglis, G. N., Badger, M. P. S., Naafs, B. D. A., Behrooz, L., Remmelzwaal, S., et al. (2017). Hydrological and associated biogeochemical consequences of rapid global warming during the Paleocene-Eocene Thermal Maximum. *Global and Planetary Change*, *157*, 114–138. https://doi.org/10.1016/j.gloplacha.2017.07.014

Champion, S. M. E., White, N. J., Jones, S. M., & Lovell, J. P. B. (2008). Quantifying transient mantle convective uplift: An example from the Faroe-Shetland basin. *Tectonics*, *27*(1), TC1002. https://doi.org/10.1029/2007TC002106

Charles, A. J., Condon, D. J., Harding, I. C., Pälike, H., Marshall, J. E. A., Cui, Y., et al. (2011). Constrains on the numerical age of the Paleocene-Eocene boundary. *Geochemistry, Geophysics and Geosystem*, *12*(6), Q0AA17. https://doi.org/10.1029/2010GC003426

Collinson, M., Steart, C. C., Harrington, G. J., Hooker, J. J., Scott, A. C., Allen, L. O., et al. (2009). Palynological evidence of vegetation dynamics in response to palaeoenvironmental change across the onset of the Paleocene–Eocene thermal maximum at Cobham, Southern England. *Grana*, *48*(1), 38–66. https://doi.org/10.1080/00173130802707980

Conway-Jones, B. W., & White, N. (2022). Paleogene buried landscapes and climatic aberrations triggered by mantle plume activity. *Earth and Planetary Science Letters*, *593*, 117644. https://doi.org/10.1016/j.epsl.2022.117644

Croudace, I. W., & Rothwell, R. G. (2015). *Micro-XRF studies of sediment cores: Applications of a non-destructive tool for the environmental sciences*. Springer Science+Business Media. https://doi.org/10.1007/978-94-017-9849-5

Cui, Y., Kump, L. R., Ridgwell, A. J., Charles, A. J., Junium, C. K., Diefendorf, A. F., et al. (2011). Slow release of fossil carbon during the paleocene-eocene thermal maximum. *Nature Geoscience*, *4*(7), 481–485. https://doi.org/10.1038/ngeo1179

Dahl, T. W., Ruhl, M., Hammarlund, E. U., Canfield, D. E., Rosing, M. T., & Bjerrum, C. J. (2013). Tracing euxinia by molybdenum concentrations in sediments using handheld X-ray fluorescence spectroscopy (HHXRF). *Chemical Geology*, *360–361*, 241–251. https://doi.org/10.1016/j.chemgeo.2013.10.022

Dickson, A. J. (2017). A molybdenum-isotope perspective on Phanerozoic deoxygenation events. *Nature Geoscience*, *10*, 721–726. https://doi.org/10.1038/ngeo3028

Dickson, A. J., Cohen, A. S., & Coe, A. L. (2012). Seawater oxygenation during the paleocene eocene thermal maximum. *Geology*, *40*(7), 639–642. https://doi.org/10.1130/G32977.1

Dickson, A. J., Cohen, A. S., & Coe, A. L. (2014). Continental margin molybdenum isotope signatures from the early Eocene. *Earth and Planetary Science Letters*, *404*, 389–395. https://doi.org/10.1016/j.epsl.2014.08.004

Dickson, A. J., Idiz, E., Porcelli, D., & Van den Boorn, S. H. J. M. (2019). The influence of thermal maturity on the stable isotope compositions and concentrations of molybdenum, zinc and cadmium in organic-rich marine mudrocks. *Geochimica et Cosmochimica Acta*, *287*, 205–220. https://doi.org/10.1016/j.gca.2019.11.001

Dickson, A. J., Jenkyns, H. C., Porcelli, D., Van den Boorn, S., & Idiz, E. (2016). Basin-Scale controls on the molybdenum-isotope composition of seawater during oceanic anoxic event 2 (late Cretaceous). *Geochimica et Cosmochimica Acta*, *178*, 291–306. https://doi.org/10.1016/j.gca.2015.12.036

Dickson, A. J., Rees-Owen, R. L., März, C., Coe, A. L., Cohen, A. S., Pancost, R. D., et al. (2014). The spread of marine anoxia on the northern Tethys margin during the Paleocene-Eocene Thermal Maximum. *Paleoceanography*, *29*(6), 471–488. https://doi.org/10.1002/2014PA002629

Dunkley Jones, T., Lunt, D. J., Schmidt, D. N., Ridgwell, A., Sluijs, A., Valdes, P. J., & Maslin, M. (2013). Climate model and proxy data constraints on ocean warming across the Paleocene–Eocene Thermal Maximum. *Earth-Science Review*, *125*, 123–145. https://doi.org/10.1016/j.earscirev.2013.07.004

Eldrett, J. S., Greenwood, D. R., Polling, M., Brinkhuis, H., & Sluijs, A. (2014). A seasonality trigger for carbon injection at the Paleocene–Eocene Thermal Maximum. *Climate of the Past*, *10*(2), 759–769. https://doi.org/10.5194/cp-10-759-2014

Garel, S., Schnyder, J., Jacob, J., Dupuis, C., Boussafir, M., Le Milbeau, C., et al. (2013). Paleohydrological and paleoenvironmental changes recorded in terrestrial sediments of the Paleocene-Eocene boundary (Normandy, France). *Palaeogeography, Palaeoclimatology, Palaeoecology*, *376*, 184–199. https://doi.org/10.1016/j.palaeo.2013.02.035

Goldberg, T., Gordon, G. W., Izon, G., Archer, C., Pearce, C. R., McManus, J., et al. (2013). Resolution of inter-laboratory discrepancies in Mo isotope data: An intercalibration. *Journal of Analytical Atomic Spectrometry*, *28*(5), 724–735. https://doi.org/10.1039/C3JA30375F

Golonka, J. (2009). Phanerozoic paleoenvironment and paleolithofacies maps: Cenozoic. *Geologia/Akademia Górniczo-Hutnicza im, Stanisława Staszica w Krakowie*, *35*, 507–587.

Harding, I. C., Charles, A. J., Marshall, J. E. A., Pälike, H., Roberts, A. P., Wilson, P. A., et al. (2011). Sea level and salinity fluctuations during the Paleocene–Eocene thermal maximum in Arctic Spitsbergen. *Earth and Planetary Science Letters*, *303*(1–2), 97–107. https://doi.org/10.1016/j.epsl.2010.12.043

Hartley, R. A., Roberts, G. G., White, N., & Richardson, C. (2011). Transient convective uplift of an ancient buried landscape. *Nature Geoscience*, *4*(8), 562–565. https://doi.org/10.1038/ngeo1191

Helz, G. R., Bura-Nakić, E., Mikac, N., & Ciglenečki, I. (2011). New model for molybdenum behavior in euxinic waters. *Chemical Geology*, *284*(3–4), 323–332. https://doi.org/10.1016/j.chemgeo.2011.03.012

Helz, G. R., Miller, C. V., Charnock, J. M., Mosselmans, J. F. W., Pattrick, R. A. D., Garner, C. D., & Vaughan, D. J. (1996). Mechanism of molybdenum removal from the sea and its concentration in black shales: EXAFS evidence. *Geochimica et Cosmochimica Acta*, *60*(19), 3631–3642. https://doi.org/10.1016/0016-7037(96)00195-0

Hovikoski, J., Fyhn, M. B. W., Nøhr-Hansen, H., Hopper, J. R., Andrews, S., Barham, M., et al. (2021). Paleocene-Eocene volcanic segmentation of the Norwegian-Greenland seaway reorganized high-latitude ocean circulation. *Communications Earth & Environment*, *2*(1), 172. https://doi.org/10.1038/s43247-021-00249-w

Jin, S., Kemp, D. B., Yin, R., Sun, R., Shen, J., Jolley, D. W., et al. (2023). Mercury isotope evidence for protracted North Atlantic magmatism during the paleocene-eocene thermal maximum. *Earth and Planetary Science Letters V.*, *602*, 117926. https://doi.org/10.1016/j.epsl.2022.117926

Jones, M. T., Percival, L. M. E., Stokke, E. W., Frieling, J., Mather, T. A., Riber, L., et al. (2019). Mercury anomalies across the Palaeocene–eocene thermal maximum. *Climate of the Past*, *15*(1), 217–236. https://doi.org/10.5194/cp-15-217-2019

Jones, M. T., Stokke, W., Rooney, A. D., Frieling, J., Pogge von Strandmann, P. A. E., Wilson, D. J., et al. (2023). Tracing North Atlantic volcanism and seaway connectivity across the paleocene–eocene thermal maximum (PETM). *Climate of the Past*, *19*(8), 1623–1652. https://doi.org/10.5194/cp-19-1623-2023

Jones, S. M., Hoggett, M., Greene, S. E., & Dunkley Jones, T. (2019). Large igneous province thermogenic greenhouse gas flux could have initiated paleocene-eocene thermal maximum climate change. *Nature Communications*, *10*(5547), 1–16. https://doi.org/10.1038/s41467-019-12957-1

Kemp, S. J., Ellis, M. A., Mounteney, I., & Kender, S. (2016). Palaeoclimatic implications of high-resolution clay mineral assemblages preceding and across the onset of the Paleocene-Eocene thermal maximum, North Sea Basin. *Clay Minerals*, *51*(5), 793–813. https://doi.org/10.1180/claymin.2016.051.5.08

Kender, S., Bogus, K., Pedersen, G. K., Dybkjær, K., Mather, T. A., Mariani, E., et al. (2021). Paleocene/Eocene carbon feedbacks triggered by volcanic activity. *Nature Communications*, *12*(1), 5186. https://doi.org/10.1038/s41467-021-25536-0

Kender, S., Stephenson, M. H., Riding, J. B., Leng, M. J., Knox, R. W. O. 'B., Peck, V. L., et al. (2012). Marine and terrestrial environmental changes in NW Europe preceding carbon release at the Paleocene-Eocene transition. *Earth and Planetary Science Letters*, *353–354*, 108–120. https://doi.org/10.1016/j.epsl.2012.08.011

Kirtlan Turner, S., Hull, P. M., Kump, L. R., & Ridgwell, A. (2017). A probabilistic assessment of the rapidity of PETM onset. *Nature Communications*, *8*(1), 353. https://doi.org/10.1038/s41467-017-00292-2

Kjennerud, T., & Gillmore, G. K. (2003). Integrated Palaeogene palaeobathymetry of the northern North sea, Pet. *Geoscience Series*, *9*(2), 125–132. https://doi.org/10.1144/1354-079302-510

Knox, R. W. O. 'B. (1996). Correlation of the early Paleogene in northwest Europe: An overview, Sp. In R. W. O. 'B. Knox, R. M. Corfield, & R. E. Dunay (Eds.), *Correlation of the early Paleogene in northwest Europe* (Vol. 101, pp. 1–11). Geological Society Special Publication. https://doi.org/10.1144/GSL.SP.1996.101.01.01

Lenz, O. K., & Riegel, W. (2001). Isopollen maps as a tool for the reconstruction of a coastal swamp from the Middle Eocene at Helmstedt (Northern Germany). *Facies*, *45*(1), 177–194. https://doi.org/10.1007/BF02668111

Liu, Z., Horton, D. E., Tabor, C., Sageman, B. B., Percival, L. M. E., Gill, B. C., & Selby, D. (2019). Assessing the contributions of Comet impact and volcanism toward the climate perturbations of the Paleocene-Eocene thermal maximum. *Geophysical Research Letters*, *46*(24), 14798–14806. https://doi.org/10.1029/2019GL084818

Lyons, T. W., & Severmann, S. (2006). A critical look at iron paleoredox proxies: New insights from modern euxinic marine basins. *Geochimica et Cosmochimica Acta*, *70*(23), 5698–5722. https://doi.org/10.1016/j.gca.2006.08.021

Ma, Z., Gray, E., Thomas, E., Murphy, B., Zachos, J., & Paytan, A. (2014). Carbon sequestration during the Palaeocene–Eocene thermal maximum by an efficient biological pump. *Nature Geosciences*, *7*(5), 382–388. https://doi.org/10.1038/ngeo2139

Maclennan, J., & Jones, S. M. (2006). Regional uplift, gas hydrate dissociation and the origins of the Paleocene–Eocene thermal maximum. *Earth and Planetary Science Letters*, *245*(1–2), 65–80. https://doi.org/10.1016/j.epsl.2006.01.069

Mariani, E., Kender, S., Riding, J. B., Leng, M. J., Kemp, S. J., Dybkjær, K., et al. (2024). Geochemical records (d13C, TOC, XRF, SEM, total sulfur, molybdenum isotopes, clay mineralogy) from marine sediment core E-8X, central North Sea, across the Paleocene-Eocene Thermal maximum. [Dataset]. *PANGAEA*. https://doi.org/10.1594/PANGAEA.965401

Nielsen, O. B., Rasmussen, E. S., & Thyberg, B. I. (2015). Distribution of clay minerals in the northern North Sea Basin during the Paleogene and neogene: A result of source-area geology and sorting processes. *Journal of Sedimentary Research*, *85*(6), 562–581. https://doi.org/10.2110/jsr.2015.40

Owens, J. D., Reinhard, C. T., Rohrssen, M., Love, G. D., & Lyons, T. W. (2016). Empirical links between trace metal cycling and marine microbial ecology during a large perturbation to Earth's carbon cycle. *Earth and Planetary Science Letters*, *449*, 407–417. https://doi.org/10.1016/j.epsl.2016.05.046

Pancost, R., Steart, D., Handley, L., Collinson, M. E., Hooker, J. J., Scott, A., et al. (2007). Increased terrestrial methane cycling at the Palaeocene–Eocene thermal maximum. *Nature*, *449*(7160), 332–335. https://doi.org/10.1038/nature06012

Papadomanolaki, N. M., Sluijs, A., & Slomp, C. P. (2022). Eutrophication and deoxygenation forcing of marginal marine organic carbon burial during the PETM. *Paleoceanography and Paleoclimatology*, *37*(3), e2021PA004232. https://doi.org/10.1029/2021PA004232

Pearce, C. R., Burton, K. W., Pogge van Strandmann, P. A. E., James, R. H., & Gíslason, S. R. (2010). Molybdenum isotope behaviour accompanying weathering and riverine transport in a basaltic terrain. *Earth and Planetary Science Letters*, *295*(1–2), 104–114. https://doi.org/10.1016/j.epsl.2010.03.032

Penman, D. E., & Zachos, J. C. (2018). New constraints on massive carbon release and recovery processes during the Paleocene-Eocene Thermal Maximum. *Environmental Research Letters*, *13*(10), 105008. https://doi.org/10.1088/1748-9326/aae285

Planke, S., Berndt, C., & Alvarez Zarikian, C. A., & the Expedition 396 Scientists. (2023). *Mid-Norwegian margin magmatism and paleoclimate implications. Proceedings of the International Ocean Discovery Program* (Vol. 396). International Ocean Discovery Program. https://doi.org/10.14379/iodp.proc.396.2023

Pogge von Strandmann, P. A. E., Jones, M. T., West, A. J., Murphy, M. J., Stokke, E. W., Tarbuck, G., et al. (2021). Lithium isotope evidence for enhanced weathering and erosion during the Paleocene-Eocene Thermal Maximum. *Science Advances*, *7*(42). https://doi.org/10.1126/sciadv.abh4224

Prøis, B. M. (2015). *Late Paleocene – earliest Eocene prograding system in the SW Barents sea, Department of Geosciences* (p. 76). University of Oslo. Retrieved from https://www.duo.uio.no/handle/10852/45547

Schiøler, P., Andsbjerg, J., Clausen, O. R., Dam, G., Dybkjær, K., Hamberg, L., et al. (2007). Lithostratigraphy of the Palaeogene–lower neogene succession of the Danish North Sea. *Geol. Surv. Den. Green. Bull.*, *12*, 77. https://doi.org/10.34194/geusb.v12.5249

Schoon, P. L., Heilmann-Clausen, C., Schultz, B. P., Sinninghe Damsté, J. S., & Schouten, S. (2015). Warming and environmental changes in the eastern North Sea Basin during the Paleocene–Eocene thermal maximum as revealed by biomarker lipids. *Organic Geochemistry*, *78*, 79–88. https://doi.org/10.1016/j.orggeochem.2014.11.003

Secord, R., Gingerish, P. D., Lohmann, K. C., & MacLeod, K. G. (2010). Continental warming preceding the Paleocene-Eocene thermal maximum. *Nature*, *467*(7318), 955–958. https://doi.org/10.1038/nature09441

Shaw Champion, M. E., White, N. J., Jones, S. M., & Lovell, J. P. B. (2008). Quantifying transient mantle convective uplift: An example from the Faroe-Shetland basin. *Tectonics*, *27*(1), TC1002. https://doi.org/10.1029/2007TC002106

Sluijs, A., & Brinkhuis, H. (2009). A dynamic climate and ecosystem state during the paleocene–eocene thermal maximum: Inferences from dinoflagellate cyst assemblages on the New Jersey shelf. *Biogeosciences*, *6*(8), 1755–1781. https://doi.org/10.5194/bg-6-1755-2009

Sluijs, A., Brinkhuis, H., Schouten, S., Bohaty, S. M., John, C. M., Zachos, J. C., et al. (2007). Environmental precursors to light carbon input at the Paleocene/Eocene boundary. *Nature*, *450*(7173), 1218–1221. https://doi.org/10.1038/nature06400

Sluijs, A., Röhl, U., Schouten, S., Brumsack, H. J., Sangiorgi, F., Sinninghe Damste, J. S., & Brinkhuis, H. (2008). Arctic late paleocene-early eocene paleoenvironments with special emphasis on the paleocene-eocene thermal maximum (Lomonosov Ridge, Integrated ocean drilling Program Expedition 302). *Paleoceanography*, *23*, 1–17. https://doi.org/10.1029/2007PA001495

Sluijs, A., Schouten, S., Pagani, M., Woltering, M., Brinkhuis, H., Sinninghe Damsté, J. S., et al. (2006). Subtropical Arctic Ocean temperatures during the paleocene/eocene thermal maximum. *Nature*, *441*(7093), 610–613. https://doi.org/10.1038/nature04668

Stokke, E. W., Jones, M. T., Riber, L., Haflidason, H., Midtkandal, I., Schultz, B. P., & Svensen, H. H. (2021). Rapid and sustained environmental responses to global warming: The paleocene–eocene thermal maximum in the eastern North Sea. *Climate of the Past*, *17*(5), 1989–2013. https://doi.org/10.5194/cp-17-1989-2021

Stokke, E. W., Jones, M. T., Tierney, J. E., Svensen, H. H., & Whiteside, J. H. (2020). Temperature changes across the paleocene-eocene thermal maximum – A new high-resolution TEX_{86} temperature record from the eastern North Sea basin. *Earth and Planetary Science Letters*, *544*, 116388. https://doi.org/10.1016/j.epsl.2020.116388

Storey, M., Duncan, R. A., & SwisherIII, C. C. (2007). Paleocene-Eocene thermal maximum and the opening of the Northeast Atlantic. *Science*, *316*(5824), 587–589. https://doi.org/10.1126/science.1135274

Svensen, H., Planke, S., Malthe-Sørenssen, A., Jamtveit, B., Myklebust, R., Rasmussen Eidem, T., & Rey, S. S. (2004). Release of methane from a volcanic basin as a mechanism for initial Eocene global warming. *Nature*, *429*(6991), 542–545. https://doi.org/10.1038/nature02566

Thomas, E. (1998). The biogeography of the late Paleocene benthic foraminiferal extinction. In M. P. Aubry, S. Lucas, & W. A. Berggren (Eds.), *Late Paleocene-early Eocene biotic and climatic events in the marine and terrestrial records* (pp. 214–243). Columbia University Press.

Thomas, E. (2007). Cenozoic mass extinctions in the deep sea: What perturbs the largest habitat on Earth? In S. Monechi, R. Coccioni, & M. R. Rampino (Eds.), *Large ecosystem perturbations: Causes and consequences* (Vol. 424, pp. 1–23). Geological Society of America. https://doi.org/10.1130/2007.2424(01)

Tremblin, M., Khozyem, H., Adatte, T., Spangenberg, J. E., Fillon, C., Grauls, A., et al. (2022). Mercury enrichments of the Pyrenean foreland basins sediments support enhanced volcanism during the Paleocene-Eocene thermal maximum (PETM). *Global and Planetary Change*, *212*, 103794. https://doi.org/10.1016/j.gloplacha.2022.103794

Tribovillard, N., Algeo, T. J., Lyons, T., & Riboulleau, A. (2006). Trace metals as paleoredox an paleoproductivity proxies: An update. *Chemical Geology*, *232*(1–2), 12–32. https://doi.org/10.1016/j.chemgeo.2006.02.012

Vickers, M. L., Jones, M. T., Longman, J., Evans, D., Ullmann, C. V., Stokke, E. W., & IODP Expedition 396 Scientists. (2024). Paleocene–Eocene age glendonites from the Mid-Norwegian Margin – Indicators of cold snaps in the hothouse? *Climate of the Past*, *20*(1), 1–23. https://doi.org/10.5194/cp-20-1-2024

Wilkin, R. T., Arthur, M. A., & Dean, W. E. (1997). History of water-column anoxia in the Black Sea indicated pyrite framboid size distributions. *Earth and Planetary Science Letters*, *148*, 17–525. https://doi.org/10.1016/S0012-821X(97)00053-8

Wilkinson, C. M., Ganerød, M., Hendriks, B. W. H., & Eide, E. A. (2017). *Compilation and appraisal of geochronological data from the North Atlantic igneous Province (NAIP)* (Vol. 447, pp. 69–103). Geological Society, London, Special Publications. https://doi.org/10.1144/SP447.10

Zacke, A., Voigt, S., Joachimski, M. M., Gale, A. S., Ward, D. J., & Tütken, T. (2009). Surface-water freshening and high-latitude river discharge in the Eocene North Sea. *Journal of the Geological Society*, *166*(5), 969–980. https://doi.org/10.1144/0016-76492008-068

References From the Supporting Information

Deegan, C. E., & Scull, B. J. (1977). A standard lithostratigraphic nomenclature for the central and northern North Sea. *Represent Institute of Geological Science*, *77/25*, 36.

Horni, A. J., Hopper, J. R., Blischke, A., Geisler, W. H., Stewart, M., McDermott, K., et al. (2017). Regional distribution of volcanism within the North Atlantic Igneous Province. *Geological Society, London, Special Publications*, *447*(1), 105–125. https://doi.org/10.1144/sp447.18

Jones, S. M., & White, N. (2003). Shape and size of the starting Iceland plume swell. *Earth and Planetary Science Letters*, *216*(3), 271–282. https://doi.org/10.1016/S0012-821X(03)00507-7

Meyers, S. R., Sageman, B. B., & Lyons, T. W. (2005). Organic carbon burial rate and the molybdenum proxy: Theoretical framework and application to Cenomanian-Turonian oceanic anoxic event 2. *Paleoceanography*, *20*(2), 169–189. https://doi.org/10.1029/2004PA001068

Nadin, P., Kusznir, N., & Cheadle, M. (1997). Early tertiary plume uplift of the North Sea and Faroe–Shetland basins. *Earth and Planetary Science Letters*, *148*(1–2), 109–127. https://doi.org/10.1016/S0012-821X(97)00035-6

Nakagawa, Y., Takano, S., Firdaus, M. L., Norisuye, K., Hirata, T., Vance, D., & Sohrin, Y. (2012). The molybdenum isotopic composition of the modern ocean. *Geochemistry Journal*, *46*(2), 131–141. https://doi.org/10.2343/geochemj.1.0158

Smallwood, J. R., & Jill, C. E. (2002). The rise and fall of the Faroe–Shetland basin: Evidence from seismic mapping of the Balder formation. *Journal of the Geological Society*, *159*(6), 627–630. https://doi.org/10.1144/0016-764902-064

Thiry, M. (2000). Palaeoclimatic interpretation of clay minerals in marine deposits: An outlook from the continental origin. *Earth-Science Reviews*, *49*(1–4), 201–221. https://doi.org/10.1016/S0012-8252(99)00054-9